Energy Advances

ROYAL SOCIETY OF CHEMISTRY

COMMUNICATION

View Article Online
View Journal | View Issue

Cite this: *Energy Adv.*, 2022, 1, 677

Received 8th August 2022,
Accepted 19th September 2022

DOI: 10.1039/d2ya00211f

rsc.li/energy-advances

Single crystal Ni-rich NMC cathode materials for lithium-ion batteries with ultra-high volumetric energy density†

Ivan A. Moiseev,[a] Aleksandra A. Savina,[a] Alina D. Pavlova,[a] Tatiana A. Abakumova,[b] Vladislav S. Gorshkov,[a] Egor M. Pazhetnov[a] and Artem M. Abakumov *[a]

Nickel-rich layered transition metal oxides ($LiNi_xMn_yCo_{1-x-y}O_2$ ($x \geq 0.6$), Ni-rich NMCs) have been under intense investigation as high-energy density and low-cost positive electrode materials for Li-ion batteries. However, insufficient cyclic and thermal stability as well as low tap density hinder broad commercial application of commonly used polycrystalline Ni-rich NMCs. Here, we report on single crystal Ni-rich NMCs with improved cycling stability and ultra-high tap density up to 3.0 g cm^{-3} coupled with high discharge capacity, resulting in enhanced volumetric energy density of prepared electrodes up to 2680 W h L^{-1}. Record tap density is achieved due to the formation of single crystal particles with spherical-like shapes through adjustment of the lithium chemical potential by using K_2SO_4 as a solvent during the single crystal growth. The designed single crystal NMC622 and NMC811 cathode materials are promising for applications in batteries with high specific energy and long-term cycling life.

The "single crystal" layered $LiNi_xMn_yCo_{1-x-y}O_2$ oxides (SC NMCs) are promising positive electrode (cathode) materials for advanced Li-ion batteries (LIBs) with high energy density and long cycle life that is strongly demanded for successful commercialization.[1–3] The term "single crystal" in this particular case refers to the primary particles with the size of >1–2 μm consisting of a single crystalline domain and disconnected from each other, *i.e.* not forming secondary agglomerates. The single crystal primary particles demonstrate diminished surface reactivity towards electrolyte, improved resistance to mechanical cracking and higher compacting density that contributes to increasing capacity retention and volumetric energy density.[4,5]

Among various synthesis methods of SC NMCs, the molten-salt technique provides extensive control over the size and faceting of the particles. In this method, the precursor particles (such as mixed hydroxides or carbonates of transition metals) are mixed with a lithiation agent and salt of low melting temperature taken in excessive amount. The grain growth in this molten flux proceeds through the mass transport and Ostwald ripening.[6] The resulting crystal shape is governed by a competition in the surface free energy of the major crystallographic facets {104}, {001} and {012} (as referred to the $R\bar{3}m$ α-$NaFeO_2$-type structure of the NMCs) which in turn is defined by thermodynamic parameters during the grain growth. Among them, the chemical composition of the salt, lithium chemical potential μ(Li) and partial oxygen pressure $p(O_2)$ are of key importance. Sodium-based salt promotes growth of octahedrally-shaped single crystals, whereas octahedral growth is suppressed with potassium which seemingly eliminates the differences in surface energy between the crystallographic facets.[7,8] Lowering μ(Li) favors the abundance of the (001) surface, whereas lowering $p(O_2)$ stabilizes the {104} facets.[9,10] This provides a chemical playground for adjusting the desired shape of SC NMCs. However, in case of high-capacity Ni-rich NMCs ($x \geq 0.6$) the chemical freedom to operate is significantly limited by the defect chemistry intrinsic in these materials. It is well known that the exchange of Li and Ni between their crystallographic positions (anti-site defects) is detrimental for the electrochemical performance, and suppression of the anti-site disorder requires lowering synthesis temperature and increasing $p(O_2)$ to stabilize Ni^{3+}.[11–14] Thus, μ(Li) remains the main parameter to affect the crystal morphology of Ni-rich SC NMCs.

Acquiring control over the particle shape becomes particularly important if the volumetric energy density and, hence, tap and compact densities of SC NMCs have to be maximized. The densest random packing of ~64–70% is achieved for spherical or elliptical particles,[15] whereas the faceted particles with sharp corners and edges tend to link with each other into laced structures.

[a] *Center for Energy Science and Technology, Skolkovo Institute of Science and Technology, Nobel Str. 3, 121205, Moscow, Russia. E-mail: a.abakumov@skoltech.ru*

[b] *Rustor Ltd, Skolkovo Innovation Center, Bolshoi blv 43-1, 121205, Moscow, Russia*

† Electronic supplementary information (ESI) available. See DOI: https://doi.org/10.1039/d2ya00211f

Thus, it is fully legitimate to perform a search for the parameters allowing for preparation of the round-shaped SC NMCs particles instead of the highly faceted ones. Such roundish crystals can be shaped with a large number of various vicinal surfaces arising due to reduced surface energy anisotropy, *i.e.* diminished energy difference between the major crystallographic facets {104}, {001} and {012}. Herein, we report on the single crystal $LiNi_{0.8}Mn_{0.1}Co_{0.1}O_2$ (SC811) and $LiNi_{0.6}Mn_{0.2}Co_{0.2}O_2$ (SC622) materials with spherical or spherical-like primary particles obtained *via* molten-salt synthesis by adjusting μ(Li) in the melt through finding the right $LiOH/K_2SO_4$ ratio.

The single crystal SC622 and SC811 were synthesized *via* the molten-salt method using K_2SO_4 as a solvent. The synthesis procedure is described in detail in ESI.† Typically, mixed hydroxide precursors $Ni_{0.6}Mn_{0.2}Co_{0.2}(OH)_2$ and $Ni_{0.8}Mn_{0.1}Co_{0.1}(OH)_2$ were prepared *via* a co-precipitation and then annealed with $LiOH{\cdot}H_2O$ and K_2SO_4 as a molten-salt mixture at 900 °C. In addition, the precursors were annealed replacing $LiOH{\cdot}H_2O$ with Li_2CO_3 (samples are named as SC622_100 and SC811_100) and with the Li_2CO_3 : $LiOH{\cdot}H_2O$ = 50 : 50 mixture (samples SC622_50 and SC811_50) at the same conditions in order to estimate the influence of Li_2CO_3/LiOH ratio on the resulting morphology. The flux was removed by a water-washing step followed by drying and final annealing at 700 °C. As a reference, polycrystalline spherically-agglomerated NMC622 (PC622) and NMC811 (PC811) were prepared from the same precursors by annealing with $LiOH{\cdot}H_2O$ in two steps, first at 500 °C and then at 850 °C in air for PC622 and at 750 °C in oxygen for PC811.

In contrast to the highly faceted SC NMCs particles usually produced with the molten-salt method[7,8,16–19] the obtained SC622 and SC811 samples consist of spherical or spherical-like particles with the size distribution of D10/D50/D90 = 3.4/6.4/12.2 μm and D10/D50/D90 = 3.2/7.0/13.2 μm, respectively (Fig. 1 and Fig. S1, ESI†). For comparison, the polycrystalline PC622 and PC811 materials are made of 10–12 μm spherical agglomerates built of micron-sized and submicron primary particles, respectively (Fig. S2, ESI†). All single crystal materials

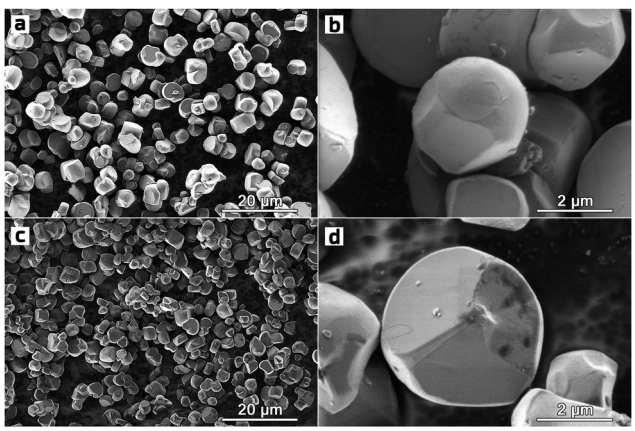

Fig. 1 Overview and high magnification SEM images of the SC622 (a and b) and SC811 (c and d) samples.

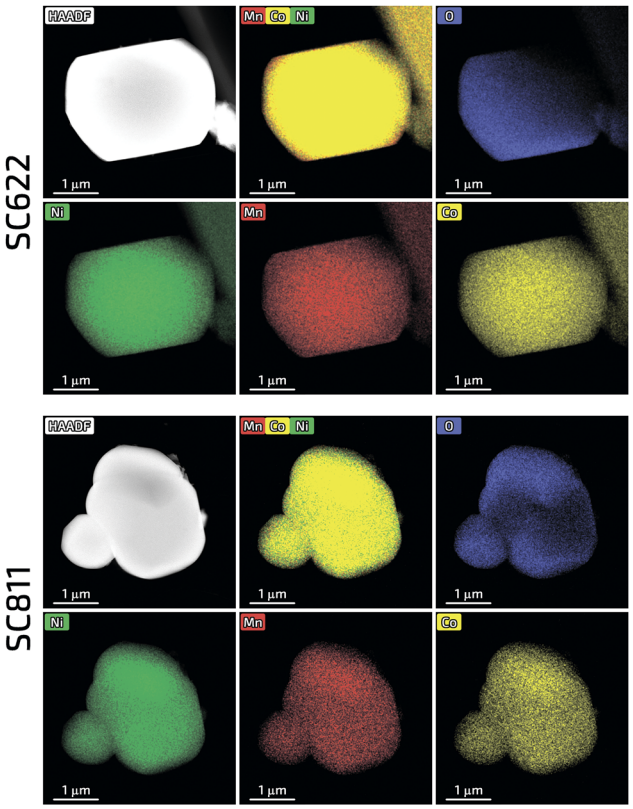

Fig. 2 HAADF-STEM images along with the color-coded elemental maps and the mixed EDX maps for Ni, Mn and Co for the SC622 and SC811 samples.

obtained using Li_2CO_3 and Li_2CO_3/LiOH mixture (SC622/811_100 and SC622/811_50) form separate particles with octahedral and prismatic shapes (Fig. S3, ESI†) with an average particle size of 1–4 microns (Fig. S3, S4 and Table S1, ESI†) as widely described in literature. To sum up, the change in the lithium source leads to loss of the spherical-like morphology. Thus, these samples are not further discussed here. The formation of impurity-free highly-ordered hexagonal α-$NaFeO_2$-type layered structure (space group $R\bar{3}m$) was validated for all the samples *via* powder X-ray diffraction (PXRD) (Fig. S5, ESI†). Rietveld refinement of the crystal structures from PXRD data revealed that the single crystal materials possess only tiny amount of Li^+/Ni^{2+} cation exchange (0.8–1.2%), which is considerably lower than that for their polycrystalline analogues (1.9–2.4%) (Table S2, ESI†). The homogeneous distribution of Ni, Mn, and Co in all samples was confirmed by energy-dispersive X-ray analysis in a scanning transmission electron microscope (STEM-EDX, Fig. 2 and Fig. S6, ESI†). The quantified cationic compositions of the obtained materials correspond well to their nominal stoichiometries (Table S3, ESI†). In addition, the water-washing step turned out to be effective in removing K_2SO_4 used as flux salt since no sulfur and potassium impurities were detected in the SC622 and SC811 samples by both PXRD and STEM-EDX analysis (Fig. S7, ESI†).

X-Ray photoelectron spectroscopy (XPS) analysis was used to reveal oxidation state of transition metals. The representative

XPS spectra for Ni, Mn and Co are demonstrated in Fig. S8 (ESI†). Further we provide a detailed analysis for Ni as an element present in +2/+3 oxidation states depending on the NMC's chemical compositions, while the description of the spectra for Mn and Co are given in ESI.† Ni2p$_{3/2}$ photoelectron spectra are usually complex and display numerous components,[20] while charging effect in photoelectron process and photoelectron energy losses on surface contaminations (Li hydroxide and carbonate) give additional distortions. In our case, the XPS spectra (Fig. S8, ESI†) show that both Ni^{2+} and Ni^{3+} are present at the surface of the all SC622/811 and PC622/811 samples, with predominance of Ni^{3+}. This is evidenced by the main peak maximum at 855.3 eV (SC622 and PC622) and 855.7 eV (SC811 and PC811), and an additional broad loss peak at 861.5 eV. For Ni^{3+} this loss peak is shallow relatively to that for Ni^{2+} that we indeed found in our samples, whereas for high concentration of Ni^{2+} this loss peak should be much more pronounced.[21] For both samples with high nickel concentration (SC811 and PC811) asymmetry of the main peak was detected with shift of the peak's maximum from 855.3 eV (SC622 and PC622) to 855.7 eV (SC811 and PC811). The asymmetry is a typical feature of Ni^{3+}, indicating considerable increase in Ni^{3+} amount on going from 622 to 811 compositions.

The tap density, measured using a tapped density analyzer, reaches 3.0 g cm^{-3} and 2.9 g cm^{-3} for the SC622 and SC811 materials, respectively, while polycrystalline PC622 and PC811 show significantly lower values albeit typical for the polycrystalline NMC materials (Table 1).[22,23] This ultra-high tap density is achieved due to compact packing of the round-shaped single crystal particles which possess no internal porosity, in contrast to spherical secondary agglomerates in the polycrystalline samples. Besides, powder compact density of single crystal SC622 and SC811 exceeds that of previously reported octahedral SC NMCs materials[24] (Table 1).

The electrochemical performance of the obtained cathode materials was investigated in two-electrode coin-type cells with metallic Li as a counter-electrode by galvanostatic charge/discharge tests in the potential range of 2.7–4.3 V *vs.* Li/Li$^+$ at room temperature. The charge/discharge profiles of the SC622 and SC811 cathodes at 0.1C current density (1C = 180 mA g^{-1} for NMC622 and 200 mA g^{-1} for NMC811) are similar to those of their polycrystalline analogues (Fig. 3a and b). The single crystal

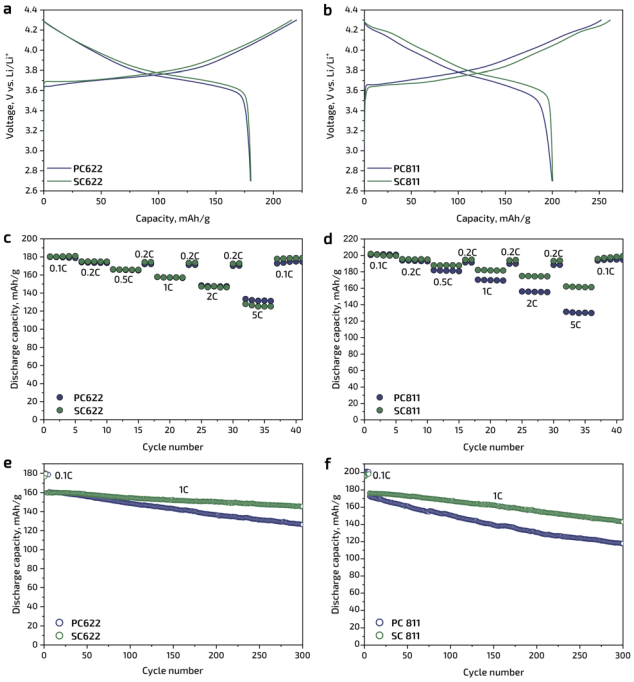

Fig. 3 Electrochemical characterization of the cathode materials: first-cycle voltage profile (a and b), rate capability tests (c and d) and cycling performance (e and f) of the single crystal SC622 and SC811 samples in comparison with their polycrystalline PC622 and PC811 analogues.

SC and polycrystalline PC samples deliver nearly the same initial discharge capacities of ~180 mA h g^{-1} for NMC622 and ~200 mA h g^{-1} for NMC811, the Coulombic efficiency of the first cycle is in the range of 82–83% for NMC622 and 76–79% for NMC811. The rate capability is similar for the single crystal and polycrystalline NMC622 samples (Fig. 3c and Table 1): the 0.1C discharge capacity of 180 mA h g^{-1} for the SC622 and PC622 is reduced to 131 and 125 mA h g^{-1} at 5C, respectively. In contrast, SC811 shows higher rate capability compared to polycrystalline PC811, providing at least 10–15% increase in discharge capacity at elevated current densities (Fig. 3d and Table 1). The enhanced rate capability may be attributed to the single crystal morphology. As Li-ion transport in NMC is essentially two-dimensional, in the polycrystalline samples the Li-ion diffusion between adjacent

Table 1 Electrochemical performance, tap density and compact density of the single crystal and polycrystalline NMC622 and NMC811 cathode materials

Sample	Discharge capacity at different current density, mA h g^{-1}						Capacity retention after 100/200/300 cycles at 1C (half-cell), %	Tap density, g cm^{-3}	Powder compact density, g cm^{-3}
	0.1C	0.2C	0.5C	1C	2C	5C			
SC622	180	175	166	158	148	125	97/94/91	3.0	3.9
PC622	180	174	165	158	148	131	93/85/80	2.4	3.3
SC811	200	195	187	182	175	162	95/88/81	2.9	3.8
PC811	200	194	182	170	156	131	87/76/70	2.3	2.7
SC622[16]	183	—	170	163	155	145	—/—/94	—	—
SC622[24]	183	—	172	166	—	150	96 (80 cycles)	2.0	3.46
SC622[25]	144	120	100	82	—	—	90/—/—	—	—
SC622[26]	—	180	—	—	—	—	—	—	—
SC622[27]	—	—	168	—	—	—	92/—/—	—	—
SC811[27]			192				78/—/—		
SC622[28]	—	162	156	152	145	—	—/—/90	2.3	3.3

primary grains may not be facile because the grains in agglomerates are randomly oriented and might not be perfectly aligned for the Li-ion migration. In the single crystal NMC particles, there is no such misalignment effect. In all cases, the samples recovered their original discharge capacity when the current density returned back to 0.1C after 36 cycles at different rates (Fig. 3c and d). Upon cycling at 1C, both SC622 and SC811 samples exhibit remarkable cycling stability and retained ~91% and ~81% of the initial capacity after 300 cycles, respectively, that is significantly higher than the capacity retention of the polycrystalline analogues amounting to ~81% in PC622 and 70% in PC811 (Fig. 3e and f). Moreover, the single crystal materials obtained in the present work demonstrate improved or comparable electrochemical performance being benchmarked against the previously reported single crystal Ni-rich NMCs with octahedral morphology[16,23–26] (Table 1). For instance, being cycled at 1C rate, SC811 synthesized within this work shows increased capacity retention (95% after 100 cycles) in comparison with single crystal NMC811 reported in the literature (78% after 300 cycles).[25] The SC622 material with spherical-like morphology delivers similar discharge capacity at low C-rates compared to the previously reported NMC622 single crystals,[16,22–26] being, however, inferior at 5C rate (Table 1).

Electrochemical impedance spectroscopy (EIS) was carried out for the pristine and cycled electrodes in order to deeply evaluate electrochemical performance of the polycrystalline and single crystal materials. Nyquist plots of EIS spectra for the pristine and 300 times cycled *vs.* metallic Li electrodes are presented in Fig. S7 (ESI†) and treated as described in SI. All EIS spectra consist of two semicircles at high and low frequency regions. Pristine SC622 and PC622 samples demonstrate close R_{SEI} (54.0 Ω and 47.5 Ω) and R_{ct} (89.3 Ω and 91.0 Ω), respectively. After 300 cycles R_{SEI} for SC622 and PC622 increases only slightly, to 56.3 Ω and 60.3 Ω, respectively, whereas R_{ct} grows substantially amounting to 220.4 Ω in SC622 and to 300.5 Ω in PC622. Similar tendency also exists for the SC/PC811 samples. Pristine SC/PC811 materials demonstrate R_{SEI} of 65.8/68.9 Ω and R_{ct} of 120.7/314.1 Ω. Relatively high R_{ct} for PC811 correlates with its poor rate capability at 1C–5C rates. The cycled SC/PC811 electrodes demonstrate R_{SEI} of 91.6/106.8 Ω and R_{ct} of 182.3/454.2 Ω. Rapid increase of the R_{ct} components for the polycrystalline samples correlates with poor capacity retention in comparison with the single crystal materials.

The series of electrodes were prepared under various pressure (2, 4, 8 t cm^{-2}) for single crystal SC622, SC811 and polycrystalline PC622, PC811 to evaluate and compare their microstructure through the electrode preparation process as well as to measure their electrode compact density. Cross-sections of the prepared electrodes were studied by SEM analysis. It is clearly seen that the microstructure of polycrystalline electrodes PC622 (Fig. S8, ESI†) and PC811 (Fig. S9, ESI†) changes with increasing pressure from 2 to 8 t cm^{-2}. Secondary spherical agglomerates still could be distinguished under pressure of 2 t cm^{-2}, but completely collapse and decay under high pressure of 8 t cm^{-2}. The SC622 (Fig. S8, ESI†) and SC811 (Fig. S9, ESI†) electrodes demonstrate excellent microstructural stability under all ranges of pressures (2–8 t cm^{-2}) without any crack formation or other visible destruction. The electrode compact density was used to estimate volumetric energy density values of the prepared materials. Notably, the SC622 and SC811 materials show higher electrode compact density at pressure of 8 t cm^{-2} (3.9 and 3.8 g cm^{-3}) and volumetric energy density (2490 W h L^{-1} and 2680 W h L^{-1}, respectively) than the polycrystalline materials (2110 W h L^{-1} for PC622 and 1890 W h L^{-1} for PC811) owing to their lower compact density (3.3 and 2.7 g cm^{-3}) (Table 1 and Fig. S10, ESI†).

Comparative SEM study of the 300 times cycled electrodes (Fig. S11, ESI†) was performed to reveal the influence of prolonged cycling on the microstructure of the electrode materials. While polycrystalline agglomerates lost their shape and almost completely or partially collapsed to the level of primary particles, the crystallites of the single crystal materials retain their integrity after cycling. The particle sizes of SC622 and SC811 after cycling remain similar to those in the pristine materials (Fig. S8 and S9, ESI†).

The single crystal materials were further tested in coin-type full cells in the potential range of 1.60–2.65 V at room temperature with commercially available $Li_4Ti_5O_{12}$ (LTO) as the anode. The typical loading masses were about 3.15 mg cm^{-2}, 2.87 mg cm^{-2}, and 3.40 mg cm^{-2} for SC622, SC811, and LTO, respectively. The full cells were cycled at 1C rate in CC–CV charge/CC discharge ($1C_{CC}$–$0.05C_{CV}$/$1C_{CC}$) regime after three formation cycles at 0.1C, 0.3C, and 0.5C. Typical voltage and current profiles for the cycling tests of SC622 and SC811 are shown in Fig. 4a and c. The full cells demonstrate outstanding capacity retention of about 85% and 84% after 1000 cycles for SC622 and SC811, respectively (Fig. 4b and d). A subtle drop in capacity after long-term cycling indicates virtual absence of parasitic processes, which may include electrolyte degradation, dissolution of transition metals in the cathode, and surface reactions at the anode. The obtained data demonstrate great potential of spherically-shaped single crystal Ni-rich NMCs as

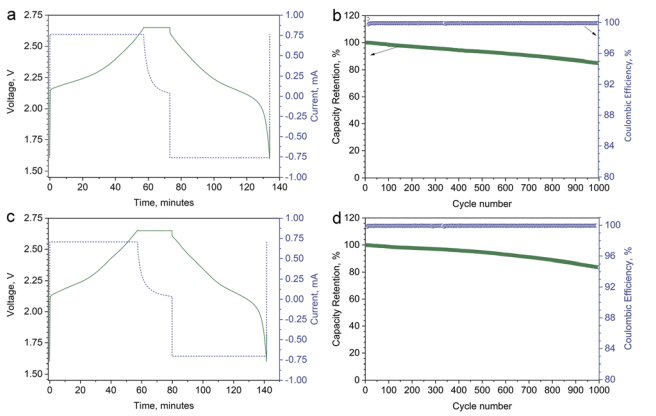

Fig. 4 Voltage and current profiles for cycling tests of SC622 (a) and SC811(c) cathode using LTO as the anode and capacity retention and Coulombic efficiency for the SC622-LTO (b) and SC811-LTO (d) full cells during long-term cycling at 1C rate.

cathode materials for Li-ion batteries with high volumetric energy density intended for long-term applications.

Conclusions

In summary, we have developed high-performance Ni-rich NMC cathode materials in the form of single crystal particles with spherical and spherical-like shapes. These materials demonstrate record tap density up to 3.0 g cm^{-3} and high discharge capacity and therefore, increased volumetric energy density compared to their polycrystalline counterparts, as well as outstanding cycling stability in both half-cell and full-cell configurations. The designed approach based on manipulation of single crystal faceting can be employed in rational design of a wide range of cathodes with better rate capability, higher volumetric energy density and cycling stability.

Author contributions

The manuscript was written through the contributions of all authors. All authors have read and agreed to the published version of the manuscript.

Conflicts of interest

The authors declare no conflict of interest.

Acknowledgements

Access to the Transmission Electron Microscopy (TEM) facilities was granted by the Advanced Imaging Core Facility (AICF) of Skoltech. This research was funded by the Russian Science Foundation, grant 20-13-00233.

Notes and references

1 J. Li, A. R. Cameron, H. Li and S. Glazier, *et al.*, *J. Electrochem. Soc.*, 2017, **164**, A1534.
2 H. Li, J. Li, X. Ma and J. R. Dahn, *J. Electrochem. Soc.*, 2018, **165**, A1038.
3 J. Kim, H. Lee, H. Cha, M. Yoon, M. Park and J. Cho, *Adv. Energy Mater.*, 2017, **8**, 1702028.
4 J. Langdon and A. Manthiram, *Energy Storage Mater.*, 2021, **37**, 143.
5 Y. Wang, E. Wang, X. Zhang and H. Yu, *Energy Fuels*, 2021, **35**, 1918.
6 T. Wang, K. Ren, M. He and W. Dong, *et al.*, *Front. Chem.*, 2020, **8**, 747.
7 T. Kimijima, N. Zettsu and K. Teshima, *Cryst. Growth Des.*, 2016, **16**, 2618.
8 Y. Kim, *ACS Appl. Mater. Interfaces*, 2012, **4**, 2329.
9 J. C. Garcia, J. Bareno, J. H. Yan and G. Y. Chen, *et al.*, *J. Phys. Chem. C*, 2017, **121**, 8290.
10 J. Zhu and G. Chen, *J. Mater. Chem. A*, 2019, **7**, 5463.
11 K. Kang, Y. Meng, J. Bréger, C. Grey and G. Ceder, *Science*, 2006, **311**, 977.
12 H. Yu, Y. Qian, M. Otani, D. Tang, S. Guo, Y. Zhu and H. Zhou, *Energy Environ. Sci.*, 2014, **7**, 1068.
13 S. Zhang, *Energy Storage Mater.*, 2019, **24**, 247.
14 E. Orlova, A. Savina, S. Abakumov, A. Morozov and A. Abakumov, *Symmetry*, 2021, **13**, 1628.
15 G. Delaney, J. Hilton and W. Cleary, *Phys. Rev. E: Stat., Nonlinear, Soft Matter Phys.*, 2011, **83**, 051305.
16 G. Qian, Y. Zhang, L. Li, R. Zhang, J. Xu and Z. Cheng, *Energy Storage Mater.*, 2020, **27**, 140.
17 Y. Zong, Z. Guo, T. Xu, C. Liu, Y. Li and G. Yang, *Int. J. Energy Res.*, 2020, **44**, 5538.
18 T. Kimijima, N. Zettsu and K. Teshima, *Cryst. Growth Des.*, 2016, **16**, 2618.
19 R. Liang, Z.-Y. Wu, W.-M. Yang, Z.-Q. Tang, G.-G. Xiong, Y.-C. Cao, S.-R. Hu and Z.-B. Wang, *Ionics*, 2020, **26** 1635.
20 A. Grosvenor, M. Biesinger, R. Smart and N. McIntyre, *Surf. Sci.*, 2006, **600**, 1771.
21 Z. Fu, J. Hu, W. Hu, S. Yang and Y. Luo, *Appl. Surf. Sci.*, 2018, **441**, 1048.
22 G. Liu, M. Li and N. Wu, *et al.*, *J. Electrochem. Soc.*, 2018, **165**, A3040.
23 B. Pei, H. Zhou and A. Goel, *et al.*, *J. Electrochem. Soc.*, 2021, **168**, 050532.
24 G. Qian, Z. Li and D. Meng, *et al.*, *J. Electrochem. Soc.*, 2021, **168**, 010534.
25 L. Zheng, *et al.*, *J. Electrochem. Soc.*, 2020, **167**, 130536.
26 H. Li, J. Li, X. Ma and J. R. Dahn, *J. Electrochem. Soc.*, 2018, **165**, A1038.
27 A. Manthiram, B. Song and W. Li, *Energy Storage Mater.*, 2017, **6**, 125.
28 Liu Guilong, *et al.*, *J. Electrochem. Soc.*, 2018, **165**, A3040.